Electrical Engineering
https://doi.org/10.1007/s00202-023-01761-2

ORIGINAL PAPER

Fast dynamic control for a boost DC/DC converter in hybrid-electric powertrain with PEM fuel cell and battery pack

Alessandro Campanini[1] · Mattia Simonazzi[1] · Leonardo Sandrolini[1] · Claudio Rossi[1] · Marco Bosi[1]

Received: 4 May 2022 / Accepted: 22 January 2023

Abstract
When working with hybrid-electric powertrain with a proton exchange membrane fuel cell (PEMFC) along with a battery pack, to increase the life of the PEMFC and avoid a drop of performance it needs to be periodically short circuited. The periodic short circuit of the PEMFC requires the DC/DC converter to be decoupled from the PEMFC. This behaviour leads the converter to undergo several start-up transients, and for an optimal energy management, the converter must reach its reference steady-state condition as quickly as possible. In this frame, this paper presents an innovative dynamic control for current mode operations of a boost DC/DC converter for managing the power exchange between the fuel cell and the battery pack, which could be easily implemented in industrial applications. With the proposed control system, the converter achieves faster step response when turned on, reducing the time required by the controlled current to reach its set point. To support theoretical considerations and simulations results, an experimental validation has been performed with a real system prototype.

Keywords DC/DC converter · Boost converter · Control system · Current mode control · Fuel cell · Battery · Hybrid powertrain

1 Introduction

The constant increase in people and transported materials has led authorities, through strict regulations on pollutant and CO_2 emissions, to force big companies in the transportation sector (such as automotive or maritime) to push research and development towards the electrification of the everyday mobility [1–3]. In addition, recent employment of SiC and GaN devices in power electronic converters [4,5] and modern Li-ion batteries enforced the vehicle transition from fossil fuels to battery electric (BEV) and plug-in electric (PHEV) [6]. Reference [7] gives a deep overview and an analysis of the positive trend of the sales market towards this direction.

However, the increased vehicles electrification complicates the actual powertrain structure, especially when on-board devices operating at different voltage levels have to be connected together [8–11]. When considering power devices directly coupled with the DC bus, the need of controlling the power flow exchange among devices and the DC bus requires DC/DC converters. Usually, the powertrain system is commanded by a vehicle control unit (VCU), which manages the throttle and brake input reference signals by sending a reference command value to each DC/DC converter in order to match, time by time, the demanded power. Most likely the sent commands are current or power set points [12,13].

When considering an hybrid powertrain with proton exchange membrane fuel cell (PEMFC) and battery pack such as the one presented in Fig. 1, different control strategies might be implemented to manage the power split between fuel cell and battery pack.

The PEMFC might be mapped, and the total energy required by the hybrid system can be controlled according to it [14]. Another possible solution relies on a PEMFC which works as a main power source and the battery pack

✉ Alessandro Campanini
alessandro.campanini@unibo.it

Mattia Simonazzi
mattia.simonazzi2@unibo.it

Leonardo Sandrolini
leonardo.sandrolini@unibo.it

Claudio Rossi
claudio.rossi@unibo.it

Marco Bosi
marco.bosi7@unibo.it

[1] Department of Electrical, Electronic, and Information Engineering, University of Bologna, Via del Risorgimento 2, Bologna 40136, Italy

Published online: 04 February 2023

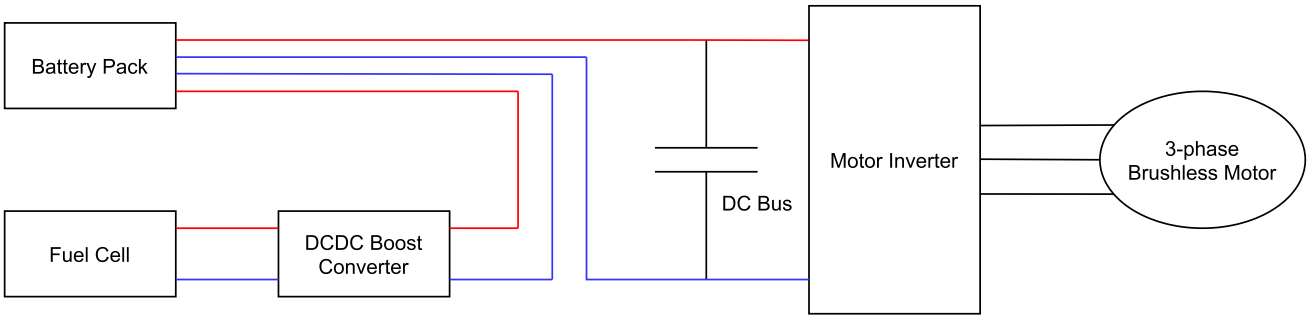

Fig. 1 Powertrain layout. The bus DC what feeds the motor inverter is directly coupled with the battery pack, while it is connected to the fuel cell through a boost DC/DC converter

acts as an energy balancer to match the load request [15], or more complex architectures with multiple loads that require particular converter topologies [16]. Moreover, the energy management could also be focused on reducing fuel cell consumption and degradation [17]. Another possible solution consists in enforcing the PEMFC to operate in the condition of maximum efficiency. As a consequence, if the demanded power is greater than the one available from the PEMFC, the battery will contribute providing the missing power. On the other hand, when the demanded power is lower than the one generated by the PEMFC, the excess of power will charge the battery, according to the state of charge (SOC) availability. Another type of strategy consists in keeping the battery state of charge in a well-defined range, as it happens for typical PHEV applications. However, PEMFCs always require to be short circuited periodically, independently of the adopted control strategy [18]. Due to the voltage levels involved in the powertrain architecture, the DC/DC required to control the PEMFC relies on the boost family. Reference [19,20] provides a control technique based on a fuzzy logic controller. When adopting this control technique, the performance of the controller strongly depends on the choice of membership functions and on the inference of fuzzy rules. On the other hand, it does not require an accurate mathematical model of a power converter, which is required in algorithms such as Model Reference Adaptive Controller (MRAC) [21] and h-infinitive controller [22]. Model predictive control (MPC) [23] and MPC based on sliding mode observer [24,25] are also well known in the literature for their satisfactory responses. However, all the techniques above mentioned require a really accurate knowledge of the converter and its parameters. In addition, their accuracy is also affected by the converter modelling. Therefore, when working in industrial application with limited resources available on the microcontroller, they might not be the best solution. On top of that, this paper presents an innovative and optimized control technique for the turn-on of boost converters subjected to periodically start-up transients, while the step-down behaviour still corresponds to the classical first-order R-L circuit response of the converter. The structure of this manuscript is organized as follows: Section 2 provides an overall description of the system, analysing the performance of a PEMFC during a real working cycle and illustrating the adopted battery model and characterization procedure. The choice of the selected converter topology is also motivated. Section 3 describes the converter control system, proposing an improved control technique and including a discussion of the different solutions presented in the literature. The dynamic behaviour of the control schemes has been simulated and is analysed in Sect. 4, while the effectiveness of the improved control strategy is experimentally verified in Sect. 5. Finally, Section 6 concludes this paper reporting the results alongside providing a quantitative comparison of system responses according to the proposed control strategies.

2 System description

In the powertrain system considered in this paper, which is reported in Fig. 1, the power extracted from the PEMFC and injected into the DC bus is controlled by a DC/DC boost converter driven by the VCU. Considering a battery pack with nominal voltage equal to 48 V and a PEMFC with maximum efficiency at 38 V, the boost converter must be placed in between them. When the PEMFC is placed into the powertrain architecture such the one in Fig. 2, a short-circuit unit (SCU) is usually provided along with the PEMFC by the supplier, as in case of "Horizon 2000W PEM Fuel Cell". Basically, it decouples the PEMFC from the system and the expected behaviour is to short circuit only the PEMFC avoiding to short circuit the input side of the boost converter.

Among many possible power split control strategies, the one adopted for this analysis guarantees the PEMFC to work at its maximum efficiency. In particular, the VCU receives time by time a power reference value from the pilot and controls the converter so that the power is split automatically between the PEMFC and the battery pack. To operate the converter in current mode control, a suitable current refer-

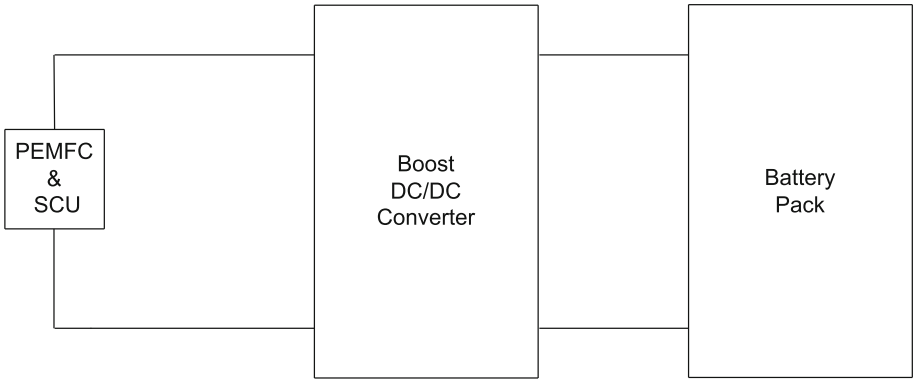

Fig. 2 Suitable PEMFC and SCU integration into hybrid powertrain architectures

ence value is required. It is defined as the ratio between the power reference received by the VCU and the PEMFC voltage, which are both sent to the boost converter and measured leading the converter, the PEMFC and the inverter motor to operate in a safe and reliable environment. The battery will be in charge of either providing or absorbing the remaining power; in case the motor power request is greater or lower than the one generated by the PEMFC, respectively.

2.1 PEMFC performance analysis

A typical efficiency-power curve of a 2 kW PEMFC is shown in Fig. 3 and exhibits a nonlinear trend in the whole power range. According to it, after the optimum point is reached the efficiency decreases up to the maximum power delivery point. Although the arbitrariness of the choice of the operating point, any solution presents efficiency benefits when adopting short-circuit methods to improve the performance of the membrane [26]. This is due to the fact that proton exchange membranes suffer from the reduction of electrochemical active surface area due to the oxidation of platinum catalyst on its electrodes. Figure 4 illustrates the experimental PEMFC short-circuit voltage for a typical working mode, including short-circuit events, applied to "Horizon 2000W PEM Fuel Cell". The SCU shorts circuit the PEMFC for 100ms each 10s, and the operating point is chosen to be the one that maximizes the efficiency, which corresponds to a nominal voltage at about 38 V.

2.2 Battery characterization

A proper modelling of the battery is essential for an accurate design of the anti-wind-up saturation limits of the regulators, and it is performed as suggested in [27,28]. Although a lithium-ion cell can be represented by several chemical [29,30], electric [31] or electro-chemical [32] models, for the aim of this paper it is straightforward to simplify the load by means of a variable voltage generator, where the battery voltage ranges from $V_{\text{batt,min}} = 37\,\text{V}$ to $V_{\text{batt,max}} = 60\,\text{V}$ with a rated voltage equal to $V_{\text{batt,rated}} = 48\,\text{V}$, as shown in Fig. 5. The battery pack is composed of a 14S-22P 21650 cylindrical cells with a rated voltage of 3.6 V and rated capacity of 3450 mAh.

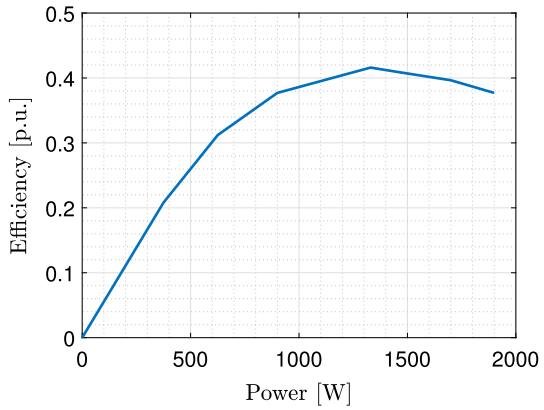

Fig. 3 Experimental efficiency-power curve obtained from the Horizon 2000W PEM Fuel Cell. Maximum efficiency is found to be at about 1350 W

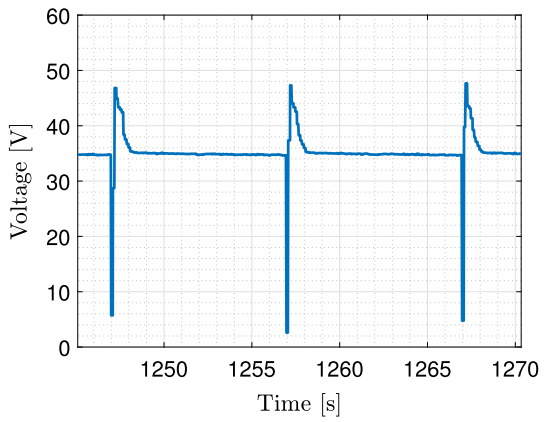

Fig. 4 Horizon 2000W PEM Fuel Cell voltage $v_{fc}(t)$ during nominal operating conditions, including short-circuit events

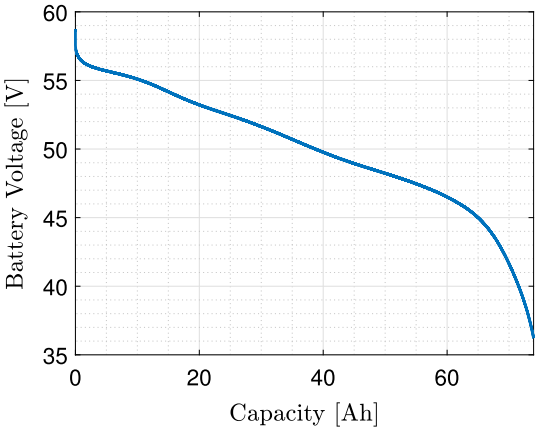

Fig. 5 Battery voltage range as a function of the capacity, for a SOC variation from 0% to 100%

2.3 Converter topology

Although many topologies of boost converters are available, when operating in real environments there are many factors to be considered, such as reliability, complexity, number of components and costs, besides, size and volume matter as well. All of these considerations suggest the convenience of adopting a converter topology that is as simple as possible and thus, in this paper, the asynchronous boost converter shown in Fig. 6 is selected. Despite the simplicity of the topology, for the discussed application the apparatus matches all the requirements.

3 Control system

Current mode operation of boost converters requires a control system able to track a reference current signal and to keep the controlled current at the desired value. With reference to the circuit depicted in Fig. 6, two scenarios are possible when using traditional boost converters, depending on whether the controlled current is the input $i_{\text{in}}(t)$ or the output $i_{\text{batt}}(t)$ one. In the following, due to the adopted energy management strategy, the controlled current is chosen to be at the input current side, since the converter is in charge to control the power exchange from the PEMFC and the DC bus. Considering Laplace transformed variables, the Kirchhoff's voltage law can be written as:

$$I_{\text{in}} = \frac{V_{\text{fc}} - V_{\text{pole}}}{R(1+\tau s)} \tag{1}$$

where V_{fc} and V_{pole} are the Laplace transformed fuel cell and pole voltages, respectively, s is the complex frequency, and

$$\tau = \frac{L}{R} \tag{2}$$

is the electric time constant of the circuit, with L being the inductance of the circuit and R its parasitic resistance.

3.1 Traditional control scheme for current mode operations (TCS)

Figure 7 illustrates the traditional control scheme (TCS) when the converter is working in current mode. Starting from the right-hand side, the low-pass filter represents the electric circuit of Fig. 6 and modelled by (1). The pole voltage V_{pole} is generated by the DC/DC chopper, which is in turn PWM controlled. To generate the duty cycle necessary to pilot the power transistor with the gate signal S_a, a reference signal is derived from a PI regulator. As it is well known, the duty cycle δ must be enclosed, in a fully extended range, between 0 and 1 if no saturation occurs. As a consequence, to ensure the regulator output $V_{\text{pole,ref}}$ to fall between 0 and 1 the anti-wind-up limits are coordinated with the battery voltage, allowing safe and reliable operation modes. According to it, the lower and upper anti-wind-up limits can be set to 0 and V_{batt}, respectively.

3.2 Control scheme with fuel cell voltage disturbance compensation (FCVCCS)

The main drawback of the TCS can be imputed to the fuel cell voltage which appears in (1) since it acts as a disturbance entering the control scheme with positive sign in between the DC/DC chopper and the low-pass filter. Even if V_{fc} can be considered constant, there might be noise components due to signal acquisition and digital processing of acquired data. As a consequence, this disturbance would negatively affect the regulator response, since it needs also to compensate the variation of the fuel cell voltage over time, leading to an higher stress of the regulator. To increase the robustness to disturbances, when it is possible to acquire or estimate the signals, the controlled quantity can be compensated in advance by subtracting the actual contribute to the regulator's output. This solution is normally adopted for torque disturbances in electric motors. If the torque cannot be directly measured, it can be estimated through closed-loop motion experiments [33]. In our system, this technique is applied to the fuel cell voltage V_{fc} and leads to a smoother regulator response, since the V_{fc} variations are autonomously compensated.

The disturbance compensation illustrated in Fig. 8 requires to adapt the upper and lower anti-wind-up regulator limits to guarantee that the duty cycle always falls between 0 and 1. When compensating in advantage, the voltage that has to be compared with the V_{batt} does not correspond anymore with the output voltage of the regulator $V_{\text{pole,ref}}$ of Fig. 7, but it has to include the difference between the fuel cell voltage V_{fc} and the regulator output $V_{\text{pole,ref}'}$. As a consequence, the lower and the upper limits become V_{fc} and $V_{\text{batt}} + V_{\text{fc}}$, respectively.

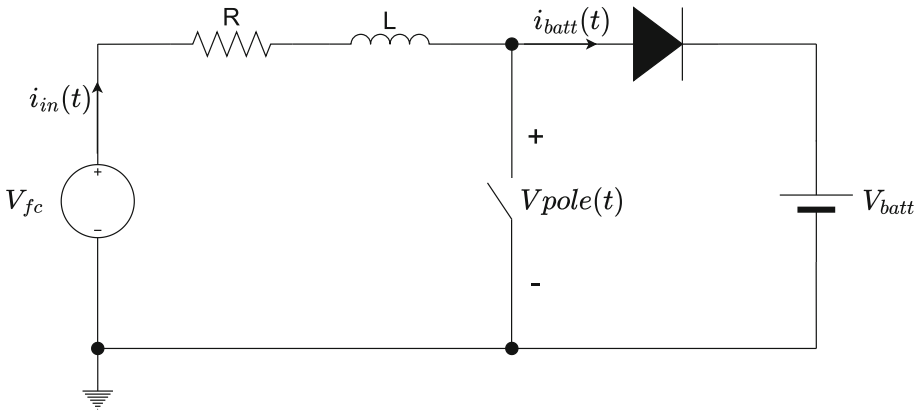

Fig. 6 Topology of the adopted boost converter

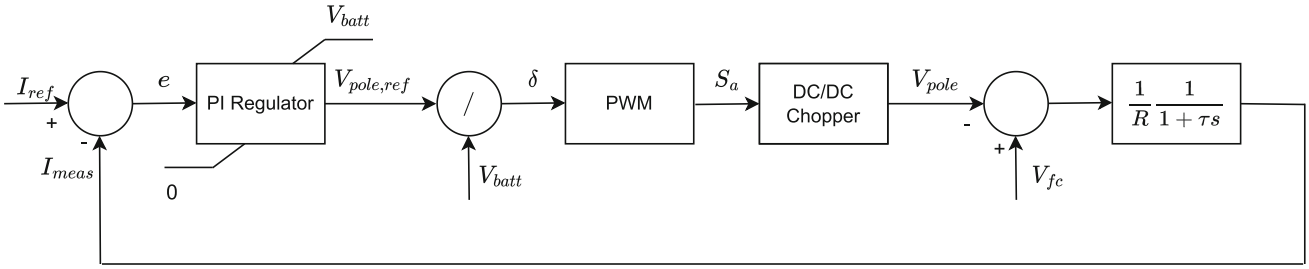

Fig. 7 Traditional control scheme for a boost converter when working in current mode operation

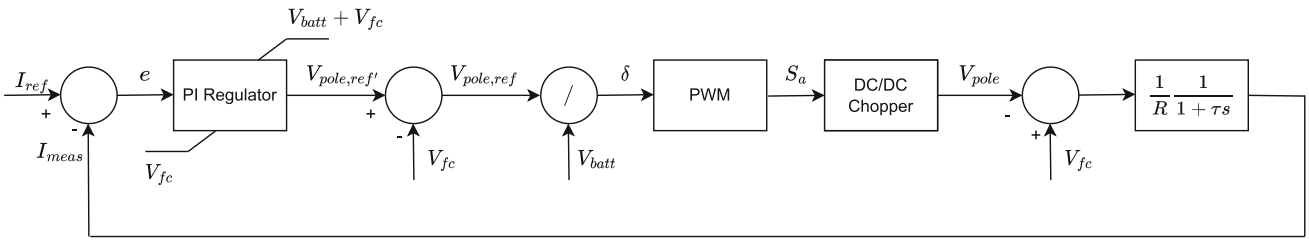

Fig. 8 Improvement of the traditional control scheme for a boost converter. It includes the fuel cell voltage disturbance compensation and the adaptation of the upper and lower anti-wind-up regulator limits

3.3 Control scheme with fuel cell voltage disturbance compensation and improved start-up dynamics (DICS)

The TCS and FCVCCS depicted in Figs. 7 and 8 still suffer from a delayed response at each start-up. When a step signal is applied, the actual current circulating on the input side of the converter requires some time to increase due to the fact that the fuel cell voltage $V_{\rm fc}$ on the left-hand side of the PWM block enters the scheme with negative sign and the regulator output keeps saturated to $V_{\rm fc}$. As a consequence, until the difference between the regulator output and the fuel cell voltage $V_{\rm pole,ref}$ is not big enough to trigger the duty cycle to increase, the control system does not start to regulate.

In order to fix that problem, the control scheme has to apply the right duty cycle as soon as the step reference signal is applied. This condition is verified when the compensated voltage $V_{\rm fc}$ enters the control scheme with positive sign. However, to hold the equivalence between the two schemes, the anti-wind-up limits need to be updated, becoming $-V_{\rm fc}$ the lower and $V_{\rm batt} - V_{\rm fc}$ the upper. It must be noticed that the gate signal S'_a obtained from the PWM block is reversed, and therefore, a not gate appears in the loop. The resulting control scheme is depicted in Fig. 9.

4 Simulations and comparison

In order to both demonstrate and highlight the differences and the validity of the presented DICS strategy, simulations are conducted according to the three configurations previously illustrated. The parameters of the physical system, the digital control system and the power electronic devices are shown in Table 1. For what concern the power switch, the system is equipped with STH310N10F7-6 100V MOSFET. Also, the free-wheeling diode of the same MOSFET is used for the output side.

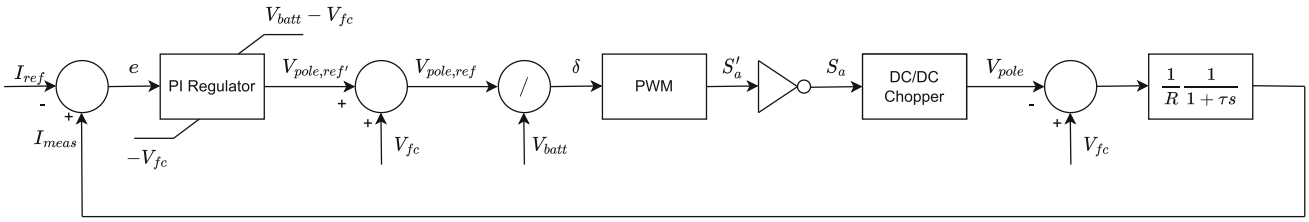

Fig. 9 Control scheme with fuel cell voltage disturbance compensation and improved start-up dynamics

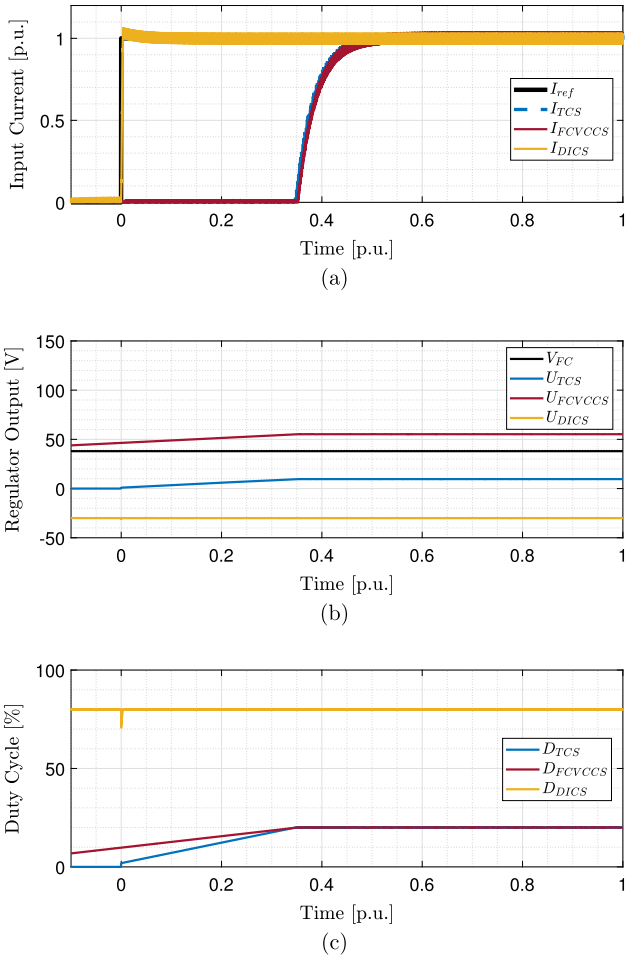

Fig. 10 Comparison of the three control schemes above described considering the normalized time scale normalized with respect to the steady-state time of the slowest transient with a margin (6 ms) and the current scale with respect to I_{ref}. It includes **a** step response analysis from 0 to I_{ref} with a zoomed box that includes the ripple behaviour in steady state, **b** regulator output behaviour, **c** duty cycle in dynamic- and steady-state value

In order to quantify the entity of the improvement and to prove the validity of the DICS, Fig. 10a compares the three step responses obtained with the TCS, FCVCCS and DICS systems, where the time scale is normalized with respect to the steady-state time of the slowest transient with a margin (6 ms) and the current with respect to the reference one, $I_{\text{ref}} = 10A$, as shown in Table 1. In order to follow the reference current value, the duty cycle applied to the power transistor inside the DC/DC chopper is calculated as

$$\delta = \frac{V_{\text{pole,ref}}}{V_{\text{batt}}}. \tag{3}$$

What is noticeable is that while the first two schemes present a certain delayed response to the reference signal when it passes from 0 to I_{ref}, the DICS immediately reacts to the current variation. For what concern the FCVCCS, this is due to the fact that $V_{\text{pole,ref}}$ could become greater than zero only when the regulator output $V_{\text{pole,ref}'}$ is greater than V_{fc}. This condition takes some time to be reached since the PI controller needs to process the signal. PI saturation ensures the duty cycle is always positive, but the converter does not start to operate until it reaches the value needed to match the requested current. Same considerations can be also applied to TCS. To avoid additional switching losses in both the TCS and FCVCCS, the actual control system of the DC/DC converter starts to modulate the power switch only when the above condition is reached. Figure 10b illustrates how the regulator output behaves in the three cases, while Fig. 10c shows the duty cycle obtained from the control schemes. Since the fuel cell voltage is supposed to be constant and equal to 38 V, the pole voltage $V_{\text{pole,ref}}$ must be approximately equal to 10 V in all cases, as the physical system is always the same. Consequently, in the TCS, the regulator output $V_{\text{pole,ref}'}$ directly corresponds to the pole voltage $V_{\text{pole,ref}}$. Instead, in the FCVCCS, the pole voltage is derived as

$$V_{\text{pole,ref}} = V_{\text{pole,ref}'} - V_{\text{fc}}, \tag{4}$$

resulting in a regulator output voltage $V_{\text{pole,ref}'} = V_{\text{pole,ref}} + V_{\text{fc}} = 55\,\text{V}$. Similar considerations can be carried out for the DICS scheme, with few differences. The first one is related to the calculation of $V_{\text{pole,ref}'}$, which is equal to $V_{\text{pole,ref}} - V_{\text{fc}}$ and thus it results in a lower value roughly equal to $-30\,\text{V}$, as shown in Fig. 10b. In addition, the duty cycle, illustrated in Fig. 10c, is complementary to 1 with respect to the one of the previous TCS and FCVCCS cases. Thus, the duty cycle starts from 1 (0.8 in this case since the saturation acts as duty

cycle limiter) as soon as the step signal is applied, resulting in a null time delay.

4.1 System dynamics

The improvement of the system dynamic response can be evaluated considering the time evolution of the average input current and pole voltage components $v_{\text{pole}}(t)$ obtained with the three control strategies above discussed. The instantaneous input current can be written as [34,35]:

$$i_{\text{in}}(t) = \bar{i}_{\text{in}}(t) + \hat{i}_{\text{in}}(t), \tag{5}$$

where $\bar{i}_{\text{in}}(t)$ is the averaged current component over the switching period and $\hat{i}_{\text{in}}(t)$ the switching current ripple component.

From the circuit depicted in Fig. 6, it can be seen that the transient behaviour of $\bar{i}_{\text{in}}(t)$ corresponds to the response of a first-order R-L circuit to a time varying voltage excitation $v(t) = V_{\text{fc}} - \bar{v}_{\text{pole}}(t)$, where $\bar{v}_{\text{pole}}(t)$ is the average component of the pole voltage $v_{\text{pole}}(t)$. Considering the excitation applied in $t = 0$, the steady state is reached when $\bar{i}_{\text{in}}(t) = I_{\text{ref}}$, namely when:

$$\frac{V_{\text{fc}} - \bar{v}_{\text{pole}}(t)}{R} = I_{\text{ref}}, \tag{6}$$

and then $\bar{i}_{\text{in}}(t)$ can be written as:

$$\bar{i}_{\text{in}}(t) = \frac{V_{\text{fc}} - \bar{v}_{\text{pole}}(t)}{R}\left(1 - e^{-\frac{t - t_d}{\tau}}\right), \tag{7}$$

where t_d is the effective time instant at which the transient starts. While the time required to reach the steady state is defined by the electric time constant τ, the initial time instant t_d and the steady-state value (through $v_{\text{pole}}(t)$) are determined by the control system and thus they are dramatically affected by the adopted control technique. In particular, with the TCS and FCVCCS described in Sects. 3.1 and 3.2, $t_d \neq 0$, thereby increasing the time required by the system to reach the steady-state value with respect to the application of the reference signal. By implementing the optimized control strategy proposed in Sect. 3.3, it is possible to have $t_d = 0$, resulting in a faster dynamics of the whole system.

In order to evaluate the actual improvement, it is possible to compare the behaviour of $\bar{i}_{\text{in}}(t)$ obtained with the three different control strategies, whose analytical expression has the form of (7). By fitting the currents resulting from the simulations with second-order exponential functions, it is found that one exponential term is sufficient to faithfully approximate the curves, which correspond to first-order transients with constant excitation.

Table 1 System parameters. It includes operating input and output voltages, boost DC/DC chopper parameters along with control system settings

Quantity	Symbol	Value	Unit of measure
Fuel cell rated voltage	V_{fc}	38	V
Battery pack rated voltage	V_{batt}	48	V
Battery pack equivalent resistance	R_0	1.2–2.7	Ω
Boost input inductance	L	50	μH
Parasitic resistance of the inductor	R	5.5	mΩ
MOSFET drain–source resistance	R_{DS}	1.9	mΩ
Diode forward voltage	V_{sd}	1.5	V
Duty cycle range	δ	0–80	%
Switching frequency	f_s	30	kHz
Reference current	I_{ref}	10	A
Proportional coefficient of the PI regulator	K_p	0.2277	–
Integral coefficient of the PI regulator	K_i	2.5	–

Table 2 Interpolation parameters

Symbol	Value [p.u.]
TCS	
a	1.006
b	$-6.45{\cdot}10^{-5}$
c	−0.9688
d	−19.57
t_d	0.34
FCVCCS	
a	1.006
b	$-6.45{\cdot}10^{-5}$
c	−0.9688
d	−19.57
t_d	0.35
DICS	
a	1.002
b	$-3.11{\cdot}10^{-4}$
c	−1.14
d	−508.42
t_d	0

The interpolating function $\tilde{\bar{i}}_{\text{in}}(t)$ is defined as:

$$\tilde{\bar{i}}_{\text{in}}(t) = ae^{b(t-t_d)} + ce^{d(t-t_d)}, \tag{8}$$

where a, b, c and d are the fitting parameters numerically determined. They are reported in Table 2 for the currents

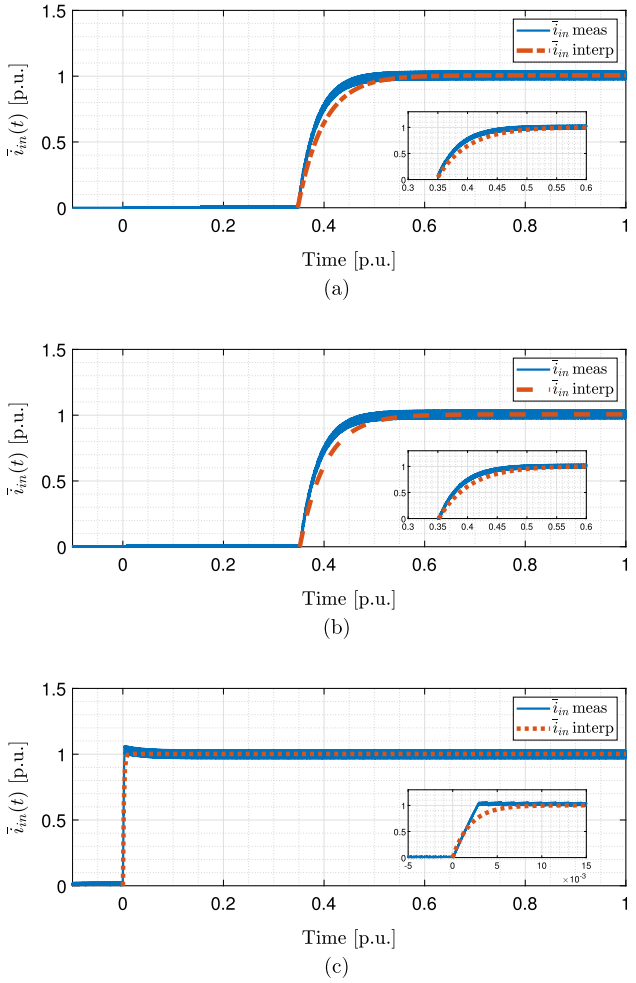

Fig. 11 Measured and interpolated trends of the average input current $\bar{i}_{\text{in}}(t)$ in case of **a** FCVCCS, **b** TCS and **c** DICS. The reference step current is applied in $t = 0$. The zoomed box represents the steady state ripple of the measured input current. The time scale is normalized with respect to the steady-state time of the slowest transient with a margin (6 ms) and the current scale with respect to I_{ref}

obtained with the three different control schemes. In particular, the parameters a and c are approximately equal for each case and correspond to the amplitude of the reference step input, namely I_{ref}. The terms b and d correspond to the inverse of the time constant of the exponential function, with $b \approx 0$ for each control strategy, always considering the time scale normalized with respect to the steady-state time of the slowest transient with a margin (6 ms) and the current with respect to the reference one I_{ref}. Thus, the average current can be well fitted by a single exponential term, with steady-state value of I_{ref} and time constant $1/d$, as it can be seen from Fig. 11, where the measured and interpolated average input current is plotted for each discussed control strategy. The starting time of the transient is defined by t_d, resulting to be different from 0 only if the DICS is implemented, as discussed above. Considering the input step I_{ref} applied at $t = 0$, in case of TCS the input current can be defined as:

$$\bar{i}'_{\text{in}}(t) = I_{\text{ref}} \left(1 - e^{-\frac{t - t'_d}{\tau'}} \right), \tag{9}$$

where t'_d is the starting time delay introduced by the control and τ' the resulting time constant. Introducing the PEMFC voltage compensation, the input current becomes:

$$\bar{i}''_{\text{in}}(t) = I_{\text{ref}} \left(1 - e^{-\frac{t - t''_d}{\tau''}} \right), \tag{10}$$

with the corresponding delay time t''_d and overall time constant τ''. As it is possible to see from Fig. 11, $t''_d > t'_d$, whereas $\tau' = \tau'' = \tau_{cl}$, resulting in a slightly slower dynamic response. Similarly, also the transient response of the current in case of DICS can be described by a first-order exponential function, which is here defined as:

$$\bar{i}'''_{\text{in}}(t) = I_{\text{ref}} \left(1 - e^{-\frac{t}{\tau_{\text{imp}}}} \right). \tag{11}$$

In this case, there is no delay time and, considering the associated time constant τ_{imp}, it holds:

$$\tau_{\text{imp}} << \tau_{\text{cl}}, \tag{12}$$

and, for the considered case, $\tau_{\text{imp}} \approx \tau_{\text{cl}}/25$. The proposed control scheme reduces the effective time constant, while it completely cancels the delay time of the transient start.

The effective improvement introduced by the proposed control strategy can be fully understood considering the amount of time required to reach the steady state with reference to the instant at which the input is applied, assumed to be $t = 0$. In general, for a first-order electric circuit, the steady state is achieved after 5τ with respect to the initial time of the transient. The time required to reach the steady state in the three different cases is named as t'_{ss}, t''_{ss} and t'''_{ss} for the transients of $\bar{i}'_{\text{in}}$, $\bar{i}''_{\text{in}}$, and $\bar{i}'''_{\text{in}}$, respectively. They can be expressed as:

$$t'_{\text{ss}} = t'_d + 5\tau_{\text{cl}}, \tag{13}$$
$$t''_{\text{ss}} = t''_d + 5\tau_{\text{cl}}, \tag{14}$$
$$t'''_{\text{ss}} = 5\tau_{\text{imp}}, \tag{15}$$

and based on the simulation values reported in Table 3 it results:

$$t'''_{\text{ss}} \ll t'_{\text{ss}} < t''_{\text{ss}}, \tag{16}$$

testifying the increased system dynamics. In particular, the FCVCCS leads to the slowest step response, with a required steady-state time of 0.6 p.u., similar to the 0.59 p.u. of the TCS. With the DICS, the system can instead reach the steady state in 0.01 p.u., corresponding to a 98.3% improvement with respect to the other two control schemes. The DICS is proved to completely cut-down the delay time, while it dramatically reduces the time constant.

5 Experimental validation

The numerical results obtained from both simulations and mathematical approach have been experimentally verified with the set-up represented in Fig. 12. The PEMFC and battery pack behaviour have been obtained through two programmable AimTTi QXP1200SP 1200 W DC-power sources. An additional low voltage (LV) DC source is needed to fed the electronics of the DC/DC boost converter. The control of the converter along with data acquisition system is managed by a dashboard running on a LabVIEW program on the Laptop through a CAN bus communication system. The converter power board is equipped with STH310N10F7-6 100V MOSFETs, and it is designed to withstand to 2 kW peak power and 1 kW continuous power, considering the aluminium heat-sink board mounted on the power module. The current has been measured with a current probe Tektronix TCP302 amplified by a Tektronix TCPA 300 current probe amplifier and processed by an Agilent "Infiniium" 54855A oscilloscope with a sampling capability of 2 GSa/s and a bandwidth of 500 MHz.

The measurement results, obtained with a system whose parameters are reported in Table 1, are illustrated and compared with numerical simulations in Fig. 13. Key features are summarized in Table 4. Since the TCS and FCVCCS exhibit the same behaviour to the step response and no disturbances large enough to trigger the corrective action of the control scheme occurred, the response of the FCVCCS to step response can be considered nearly equal to the TCS, as also testified by simulations of Fig. 11 and by parameters of Table 2 obtained from the mathematical model and therefore omitted. The experimental measurements clearly show that the converter current behaves as predicted in Sect. 4.1, despite the fact that the signal is affected by some noise. When implementing the TCS, the measured current presents a small time shift of about 0.01s in advance with respect to the simulated behaviour. It can be addressed to a little mismatch in the effective values of the circuit parameters, which are also affected by parasitics that are not considered in the simulations. In case of DICS, this shift is less noticeable, even if it is still present. As expected, the DICS makes the current ready to follow the reference signal as soon as the step variation occurs, with a small overshoot that can be observed in the experimental current. Overall, the comparison between numerical simulations and measurements shows a very good

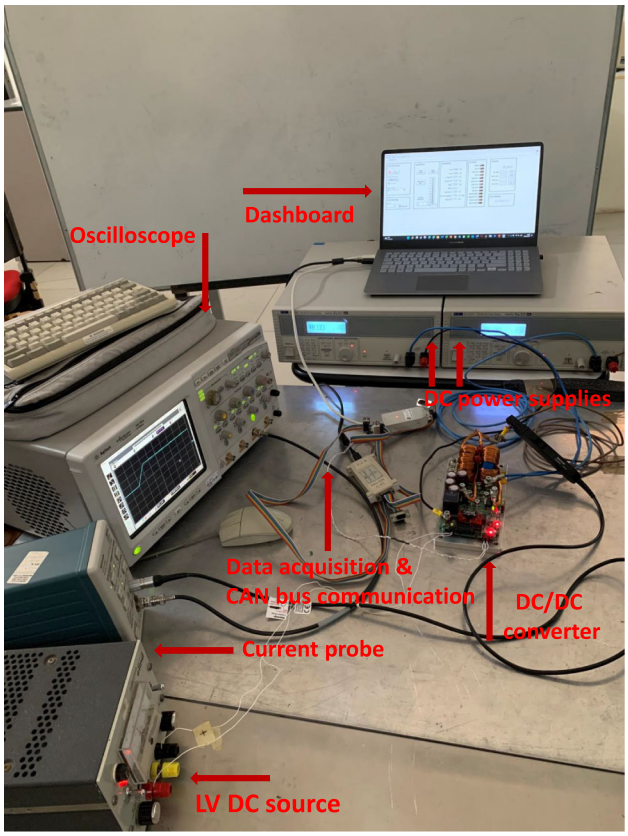

Fig. 12 Experimental set-up

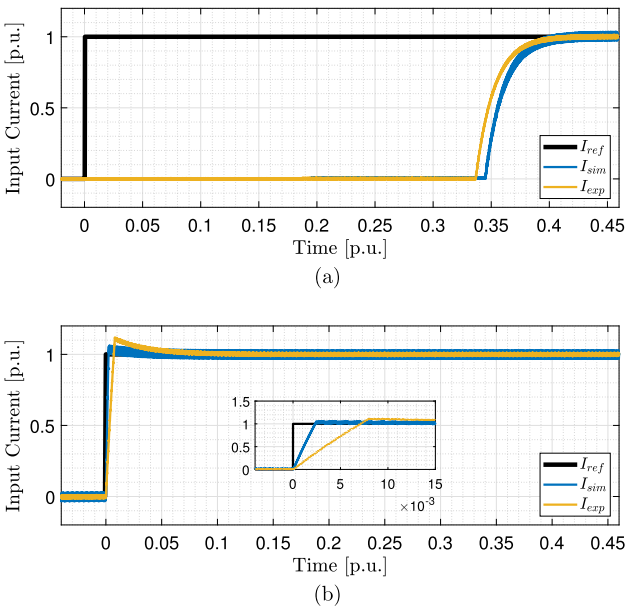

Fig. 13 Comparison between simulated and measured step responses of the converter current obtained with **a** TCS and **b** DICS. The time scale is normalized with respect to the steady-state time of the slowest transient with a margin (6 ms) and the current scale with respect to I_{ref}

Table 3 Performance comparison of the measured step response of the converter input current. The p.u. reference time is the steady-state time of the slowest transient (6 ms)

Parameter	TCS	FCVCCS	DICS	Improvement
Delay Time [p.u.]	0.34	0.35	0	100% (no delay time)
Time Constant [p.u.]	0.05	0.05	0.002	96%
Steady-State Time [p.u.]	0.59	0.6	0.01	98.3%

Table 4 Performance comparison of the measured step response of the converter input current

Parameter	TCS	DICS	Improvement
Delay Time [p.u.]	0.33	10^{-5}	100% (no delay time)
Time Constant [p.u.]	0.051	0.007	86%
Steady-State Time [p.u.]	0.585	0.04	93.2%

agreement, proving the effectiveness of the proposed method in increasing the current dynamic response with a reduction of the required steady-state time of about 93%.

6 Conclusion

Due to the electro-chemical nature of the proton exchange membrane, PEMFCs need to be periodically short circuited, requiring the DC/DC boost converter to be decoupled to the fuel cell, and thus, it undergoes several start-up transients. The current mode control of this converter can be performed according to different control strategies that have been presented, discussed and compared. The simulations have been supported by a numerical fitting of the resulting waveforms, proving that the dynamics of the overall system can be faithfully associated with one of the first-order systems and allowing the effective improvement to be quantified. Starting from the traditional control scheme, a straightforward improvement is reported, which consists in the advance compensation of the PEMFC voltage. The results clearly show that although the shape of the controlled input currents in the two cases is similar, the PEMFC voltage compensation slightly delays the starting of the transient of about 3%. Nevertheless, in the most of practical applications, this delay can be considered negligible, even though it might affect the overall behaviour of the system. However, both current waveforms obtained with and without the PEMFC voltage compensation are delayed of about 0.35 [p.u.] with respect to the instant in which the reference current signal is applied. An alternative control strategy is proposed to overcame this issue, leading to an effective and important improvement of the system dynamic response. Indeed, adopting the proposed DICS, the delay time in the transient starting is completely cancelled, whereas the resulting time constant is 130% larger with respect to the one obtained with the TCS and FCVCCS. This proves the considerable reduction in time spent by the overall system to reach the steady-state operating point. The effectiveness of the proposed DICS has been experimentally verified, and the measured signals resulted to be in very good agreement with the simulated ones, unless for a small time shift and overshoot in the current step response due to parameters mismatch. Moreover, it must be noticed that the proposed DICS can be implemented without introducing further physical sensors or altering the tuning of the PI regulator, resulting in a very simple and convenient implementation which maximizes the performance of the whole hybrid powertrain.

References

1. Conway G, Joshi A, Leach F, García A, Senecal PK (2021) A review of current and future powertrain technologies and trends in 2020. Transp Eng 5:100080
2. Diversity in transportation (2019) Why a mix of propulsion technologies is the way forward for the future fleet. Results Eng 4:100060
3. Panday A, Bansal HO (2014) Green transportation: need, technology and challenges. Int J Global Energy Issues 37(5–6):304–318
4. Ding X, Cheng J, Chen F (2017) Impact of silicon carbide devices on the powertrain systems in electric vehicles. Energies 10(4):533
5. Letellier A, Dubois MR, Trovao JP, Maher H (2015) Gallium nitride semiconductors in power electronics for electric vehicles: Advantages and challenges. In: 2015 IEEE vehicle power and propulsion conference (VPPC), pp 1–6
6. Hannan MA, Hoque MM, Hussain A, Yusof Y, Ker PJ (2018) State-of-the-art and energy management system of lithium-ion batteries in electric vehicle applications: issues and recommendations. IEEE Access 6:19362–19378
7. Khaligh A, D'Antonio M (2019) Global trends in high-power on-board chargers for electric vehicles. IEEE Trans Veh Technol 68(4):3306–3324
8. Chan CC, Chau KT (1997) An overview of power electronics in electric vehicles. IEEE Trans Ind Electron 44(1):3–13
9. Campanini A, Simonazzi M, Bosi M, Rossi C (2022) Design and comparison between psfb and llc 400/48v dc/dc stage for on-board battery charger during total and partial cc-cv charging cycles. In: 2022 IEEE 21st mediterranean electrotechnical conference (MELECON), pp 1102–1106. https://doi.org/10.1109/MELECON53508.2022.9842914
10. Ehsani M, Singh KV, Bansal HO, Mehrjardi RT (2021) State of the art and trends in electric and hybrid electric vehicles. Proc IEEE 109(6):967–984

11. Simonazzi M, Sandrolini L, Campanini A, Alberto J, Mariscotti A (2022) Center-fed resonator array for increased misalignment tolerance in automotive wireless power transfer. In: 2022 IEEE 21st mediterranean electrotechnical conference (MELECON), pp 775–779. https://doi.org/10.1109/MELECON53508.2022.9842937
12. Qiao Z, Gang L (2019) A predictive energy management system for hybrid energy storage systems in electric vehicles. Electr Eng 101:759–770
13. Sun M, Zhao P, Lin X (2022) Power management in hybrid electric vehicles using deep recurrent reinforcement learning. Electr Eng 104:1459–1471
14. Feroldi D, Serra M, Riera J (2009) Energy management strategies based on efficiency map for fuel cell hybrid vehicles. J Power Sources 190(2):387–401
15. Chao C-H, Shieh J-J (2012) A new control strategy for hybrid fuel cell-battery power systems with improved efficiency. Int J Hydrogen Energy 37(17):13141–13146 (**12th CHEC**)
16. Kumar PR, Shankar CG (2020) High-performance single-input three-output dc-dc high gain converter for fuel cell-based electric vehicles. Electr Eng 102:1715–1737
17. Upasana S, Sanjib G (2022) An energy management optimization approach for proton exchange membrane fuel cell-battery hybrid energy system for railway applications. Electr Eng 104:4179–4195
18. Dhimish M, Vieira RG, Badran G (2021) Investigating the stability and degradation of hydrogen pem fuel cell. Int J Hydrogen Energy 46(74):37017–37028
19. Ahmed B, Slami S (2017) Type-2 fuzzy logic PID controller and different uncertainties design for boost DC-DC converters. Electr Eng 99:203–211
20. Umair H, Muhammad AM, Furqan A, Aashir W, Asim K, Muhammad RJ (2022) Fuzzy logic-based voltage regulation of hybrid energy storage system in hybrid electric vehicles. Electr Eng 104:485–495
21. Shekhar A, Sharma A (2018) Review of Model Reference Adaptive Control. In: 2018 international conference on information , communication, engineering and technology (ICICET), pp 1–5. https://doi.org/10.1109/ICICET.2018.8533713
22. Swain N, Pati N (2018). Comparative Study of Model Reference Adaptive Control and H-infinity control to Non-Isolated Boost Converter. In: 2018 5th IEEE Uttar Pradesh section international conference on electrical, electronics and computer engineering (UPCON), pp 1– 4. https://doi.org/10.1109/UPCON.2018.8596833
23. Bououden S, Hazil O, Filali S, Chadli M (2014) Modelling and model predictive control of a DC-DC Boost converter. In: 2014 15th international conference on sciences and techniques of automatic control and computer engineering (STA), pp 643–648. https://doi.org/10.1109/STA.2014.7086663
24. Oettmeier FM, Neely J, Pekarek S, DeCarlo R, Uthaichana K (2009) MPC of switching in a boost converter using a hybrid state model with a sliding mode observer. IEEE Trans Ind Electron 56(9):3453–3466. https://doi.org/10.1109/TIE.2008.2006951
25. Ilhan K, Sude K, Naci G, Hasan U (2019) Design and application of pem fuel cell-based cascade boost converter. Electr Eng 101:1323–1332
26. Zhang C, Liu H, Zeng T, Chen J, Lin P, Deng B, Liu F, Zheng Y (2021) Systematic study of short circuit activation on the performance of pem fuel cell. Int J Hydrog Energy 46(45):23489–23497 (**Hydrogen Separation, Production and Storage**)
27. Simonazzi M, Campanini A, Sandrolini L, Rossi C (2021) Single stage wireless power transfer battery charger for electric vehicles. In: 2021 IEEE 15th international conference on compatibility, power electronics and power engineering (CPE-POWERENG), pp 1–6
28. Grazian F, Soeiro TB, Bauer P (2022) Inductive power transfer based on variable compensation capacitance to achieve an EV charging profile with constant optimum load. IEEE J Emerg Sel Top Power Electron. https://doi.org/10.1109/JESTPE.2022.3188060
29. Seaman A, Dao T-S, McPhee J (2014) A survey of mathematics-based equivalent-circuit and electrochemical battery models for hybrid and electric vehicle simulation. J Power Sources 256:410–423
30. Zhang X, Lu J, Yuan S, Yang J, Zhou X (2017) A novel method for identification of lithium-ion battery equivalent circuit model parameters considering electrochemical properties. Journal of Power Sources 345:21–29
31. Madani SS, Schaltz E, Knudsen Kær S (2019) An electrical equivalent circuit model of a lithium titanate oxide battery. Batteries 5(1):31
32. Nyman A, Zavalis TG, Elger R, Behm M, Lindbergh G (2010) Analysis of the polarization in a li-ion battery cell by numerical simulations. J Electrochem Soc 157(11):1236
33. Ferretti G, Magnani G, Rocco P (1998) Modeling, identification, and compensation of pulsating torque in permanent magnet ac motors. IEEE Trans Ind Electron 45(6):912–920. https://doi.org/10.1109/41.735335
34. Mandrioli R, Viatkin A, Hammami M, Ricco M, Grandi G (2021) Variable switching frequency pwm for three-phase four-wire split-capacitor inverter performance enhancement. IEEE Trans Power Electron 36(12):13674–13685
35. Hammami M, Ricco M, Viatkin A, Mandrioli R, Grandi G (2020) Evaluation of ac current ripple in case of split-capacitor three-phase four wires inverters. In: 2020 6th IEEE international energy conference (ENERGYCon), pp 128– 132